

Assessing the capability of different satellite observing configurations to resolve the distribution of methane emissions at kilometer scales

Alexander J. Turner^{1,2}, Daniel J. Jacob², Joshua Benmergui², Jeremy Brandman³, Laurent White³, and Cynthia A. Randles³

¹College of Chemistry/Department of Earth and Planetary Sciences, University of California, Berkeley, CA, USA.

²School of Engineering and Applied Sciences, Harvard University, Cambridge, Massachusetts, USA.

³ExxonMobil Research and Engineering Company, Annandale, NJ, USA.

Correspondence to: Alexander J. Turner
(alexjturner@berkeley.edu)

1 **Abstract.** Anthropogenic methane emissions originate from a large number of fine-scale and of-
2 ten transient point sources. Satellite observations of atmospheric methane columns are an attrac-
3 tive approach for monitoring these emissions but have limitations from instrument precision, pixel
4 resolution, and measurement frequency. Dense observations will soon be available in both low
5 Earth and geostationary orbits, but the extent to which they can provide fine-scale information on
6 methane sources has yet to be explored. Here we present an observation system simulation exper-
7 iment (OSSE) to assess the capabilities of different satellite observing system configurations. We
8 conduct a 1-week WRF-STILT simulation to generate methane column footprints at $1.3 \times 1.3 \text{ km}^2$
9 spatial resolution and hourly temporal resolution over a $290 \times 235 \text{ km}^2$ domain in the Barnett Shale,
10 a major oil/gas field in Texas with a large number of point sources. We sub-sample these footprints
11 to match the observing characteristics of the recently launched TROPOMI instrument ($7 \times 7 \text{ km}^2$
12 pixels, 11 ppb precision, daily frequency), the planned GeoCARB instrument ($2.7 \times 3.0 \text{ km}^2$ pixels,
13 4 ppb precision, nominal twice-daily frequency), and other proposed observing configurations. The
14 information content of the various observing systems is evaluated using the Fisher information ma-
15 trix and its eigenvalues. We find that a week of TROPOMI observations should provide information
16 on temporally invariant emissions at $\sim 30 \text{ km}$ spatial resolution. GeoCARB should provide informa-
17 tion available on temporally invariant emissions $\sim 2\text{-}7 \text{ km}$ spatial resolution depending on sampling
18 frequency (hourly to daily). Improvements to the instrument precision yield greater increases in
19 information content than improved sampling frequency. A precision better than 6 ppb is critical for
20 GeoCARB to achieve fine resolution of emissions. Transient emissions would be missed with either

21 TROPOMI or GeoCARB. An aspirational high-resolution geostationary instrument with 1.3×1.3
22 km^2 pixel resolution, hourly return time, and 1 ppb precision would effectively constrain the tem-
23 porally invariant emissions in the Barnett Shale at the kilometer scale and provide some information
24 on hourly variability of sources.

25 **1 Introduction**

26 Methane is a greenhouse gas emitted by a range of natural and anthropogenic sources (Kirschke
27 et al., 2013; Saunio et al., 2016; Turner et al., 2017). Anthropogenic methane emissions are difficult
28 to quantify because they tend to originate from a large number of potentially transient point sources
29 such as livestock operations, oil/gas leaks, landfills, and coal mine ventilation. Atmospheric methane
30 observations from surface and aircraft have been used to quantify emissions (e.g., Miller et al., 2013;
31 Caulton et al., 2014; Karion et al., 2013, 2015; Lavoie et al., 2015; Conley et al., 2016; Peischl et al.,
32 2015, 2016; Houweling et al., 2016) but are limited in spatial and temporal coverage. Satellite
33 measurements have dense and continuous coverage but limitations from observational errors and
34 pixel resolution need to be understood. Here we perform an observing system simulation experiment
35 (OSSE) to investigate the information content of different configurations of satellite instruments for
36 observing fine-scale and transient methane sources, taking as a test case the oil/gas production sector.

37 Low-Earth orbit satellite observations of methane by solar backscatter in the shortwave infrared
38 (SWIR) have been available since 2003 from the SCIAMACHY instrument (2003–2012; Franken-
39 berg et al., 2005) and from the GOSAT instrument (2009–present; Kuze et al., 2009, 2016). SWIR
40 instruments measure the atmospheric column of methane with near-unit sensitivity throughout the
41 troposphere. SCIAMACHY and GOSAT demonstrated the capability for high-precision ($<1\%$)
42 measurements of methane from space (Buchwitz et al., 2015), but SCIAMACHY had coarse pix-
43 els ($30 \times 60 \text{ km}^2$ in nadir) and GOSAT has sparse coverage (10-km diameter pixels separated by
44 250 km). Inverse analyses have used observations from these satellite-based instruments to estimate
45 methane emissions at $\sim 100\text{-}1000 \text{ km}$ spatial resolution (e.g., Bergamaschi et al., 2009, 2013; Fraser
46 et al., 2013; Monteil et al., 2013; Wecht et al., 2014a; Cressot et al., 2014; Kort et al., 2014; Turner
47 et al., 2015, 2016a; Alexe et al., 2015; Tan et al., 2016; Buchwitz et al., 2017; Sheng et al., 2018b,a).
48 But such coarse resolution makes it difficult to resolve individual source types because of spatial
49 overlap (Maasakkers et al., 2016).

50 Improved observations of methane from space are expected in the near future (Jacob et al., 2016).
51 The TROPOMI instrument (Veefkind et al., 2012; Butz et al., 2012; Hu et al., 2016, 2018), launched
52 in October 2017, will provide global mapping at $7 \times 7 \text{ km}^2$ nadir resolution once per day. The
53 GeoCARB geostationary instrument (Polonsky et al., 2014; O’Brien et al., 2016) will be launched
54 in the early 2020s with current design values of $3 \times 3 \text{ km}^2$ pixel resolution and twice-daily return
55 time. Additional instruments are presently in the proposal stage with improved combinations of

56 pixel resolution, return time, and instrument precision (Fishman et al., 2012; Butz et al., 2015; Xi
57 et al., 2015).

58 An OSSE simulates the atmosphere as it would be observed by an instrument with a given ob-
59 serving configuration and error specification. Several OSSEs have been conducted to evaluate the
60 potential of satellite observations to quantify methane sources, but they have either been conducted
61 at coarse ($\sim 50 \times 50 \text{ km}^2$) spatial resolution (Wecht et al., 2014b; Bousserez et al., 2016) or assumed
62 idealized flow conditions (Bovensmann et al., 2010; Rayner et al., 2014). Here we use a 1-week
63 simulation of atmospheric methane with $1.3 \times 1.3 \text{ km}^2$ resolution over a $290 \times 235 \text{ km}^2$ domain to
64 simulate continuous and transient emissions in the Barnett Shale region of Texas, and from there we
65 quantify the capability of different satellite instrument configurations to resolve and quantify these
66 sources at the kilometer and hourly scales. Our choice of scales is guided by the resolution of the
67 planned satellite observations, and our choice of the Barnett Shale is guided by the availability of
68 a high-resolution emission inventory for the region (Lyon et al., 2015). The pattern and density of
69 methane emissions in the Barnett Shale is typical of other source regions in the US (Maasackers
70 et al., 2016).

71 2 High-resolution OSSE environment

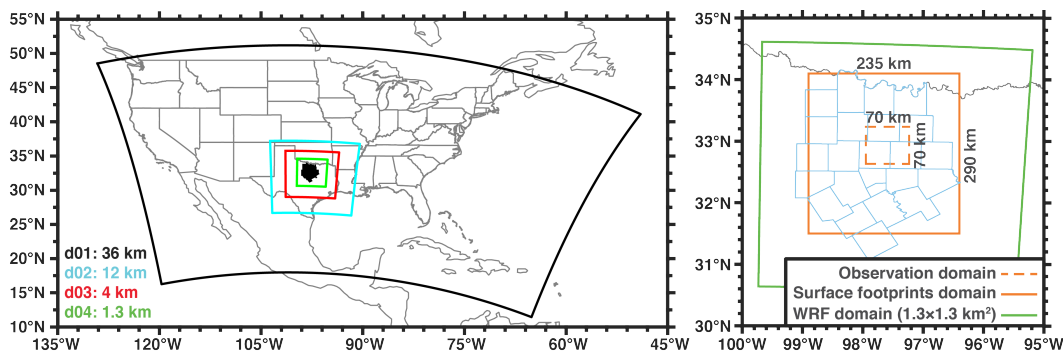


Fig. 1. High-resolution OSSE domain. Left panel shows the successive nested WRF domains at 36, 12, 4, and 1.3 km spatial resolutions, with the coarser domains providing initial and boundary conditions for the finer domains. Black shaded region is the Barnett Shale region in Texas. Right panel shows the domain for the OSSE. Green box is the innermost 1.3 km WRF domain, dashed orange box is the observation domain, solid orange box is the domain over which the footprints are computed. Light blue lines indicate the counties in the Barnett Shale.

72 We simulate atmospheric methane concentrations over the Barnett Shale in Texas at $1.3 \times 1.3 \text{ km}^2$
73 horizontal resolution for the period of October 19-25, 2013 using a framework similar to that of
74 Turner et al. (2016b). The simulation uses version 3.5 of the Weather Research and Forecasting
75 (WRF) model (Skamarock et al., 2008) over a succession of nested domains (left panel in Figure 1)

76 with $1.3 \times 1.3 \text{ km}^2$ spatial resolution in the innermost domain covering $290 \times 235 \text{ km}^2$. There are 50
 77 vertical layers up to 100 hPa. Boundary-layer physics are represented with the Mellor-Yamada-Janic
 78 scheme and the land surface is represented with the 5-layer slab model (Skamarock et al., 2008). The
 79 simulation is initialized with assimilated meteorological observations from the North American Re-
 80 gional Reanalysis (<https://www.ncdc.noaa.gov/data-access/model-data/model-datasets/north-american-regional-reanalysis-narr>).
 81 Overlapping 30-hour forecasts were initialized every 24 hours at 00 UTC and the first 6 hours of each
 82 forecast were discarded to allow for model spinup. Grid nudging was used in the outer-most domain.

83 WRF meteorology is used to drive the Stochastic Time-Inverted Lagrangian Transport (STILT)
 84 model (Lin et al., 2003). STILT is a Lagrangian particle dispersion model. It advects an ensemble
 85 of particles backward in time from selected receptor locations, using the archived hourly WRF wind
 86 fields and boundary-layer heights. STILT calculates the footprint for the receptors; a spatio-temporal
 87 map of the sensitivity of observations to emissions contributing to the concentration at each selected
 88 receptor location and time. We use STILT to calculate 10-day footprints for hourly column concen-
 89 trations at $1.3 \times 1.3 \text{ km}^2$ resolution over a $70 \times 70 \text{ km}^2$ domain in the innermost WRF nest, tracking
 90 the resulting footprints over a $290 \times 235 \text{ km}^2$ domain (right panel in Figure 1). With this system we
 91 examine the constraints on emissions over the $290 \times 235 \text{ km}^2$ domain provided by dense SWIR satel-
 92 lite observations (over the $70 \times 70 \text{ km}^2$ domain) that have up to 1.3 km pixel resolution and hourly
 93 daytime frequency. Footprints for each column are obtained by releasing 100 STILT particles from
 94 vertical levels centered at 28 m above the surface, 97 m, 190 m, 300 m, and 8 additional levels up
 95 to 14 km altitude spaced evenly on a pressure grid. The column footprints are then constructed by
 96 summing the pressure-weighted contributions from individual levels, using a typical SWIR averag-
 97 ing kernel taken from Worden et al. (2015) with near-uniformity in the troposphere, and correcting
 98 for water vapor (see Appendix A in O’Dell et al., 2012).

99 The footprint for the i^{th} receptor location and time can be expressed as a vector $\mathbf{h}_i = (\partial y_i / \partial \mathbf{x})^T$
 100 describing the sensitivity of the column concentration y at that receptor location and time to the
 101 emission fluxes \mathbf{x} over the $290 \times 235 \text{ km}^2$ domain and previous times extending up to 10 days. Here
 102 \mathbf{x} is arranged as a vector of length n assembling all the emission grid cells and hours, allowing the
 103 emissions to vary on an hourly basis. The column concentration is expressed as the dry air column-
 104 average mixing ratio (ppb) following common practice (Jacob et al., 2016). The emissions \mathbf{x} have
 105 units of $\text{nmol m}^{-2} \text{ s}^{-1}$, so that the footprint has units of $\text{ppb nmol}^{-1} \text{ m}^2 \text{ s}$. The column concentration
 106 for the i^{th} observation (y_i) can be reconstructed from its footprint as:

$$y_i = \mathbf{h}_i \mathbf{x} + b_i \quad (1)$$

107 where b_i is the background column concentration upwind of the $290 \times 235 \text{ km}^2$ domain. We can
 108 then write the full set of observations as a vector \mathbf{y} of length m , and reshape the set of m footprint
 109 vectors \mathbf{h} into an $m \times n$ sparse matrix $\mathbf{H} = \partial \mathbf{y} / \partial \mathbf{x}$ (where m is the number of observations and n is
 110 the number of state vector elements):

$$y = \mathbf{H}x + \mathbf{b} \quad (2)$$

111 where \mathbf{b} is the background vector with elements b_i and \mathbf{H} is the Jacobian matrix that maps emissions
 112 to concentration enhancements due to emissions within our domain.

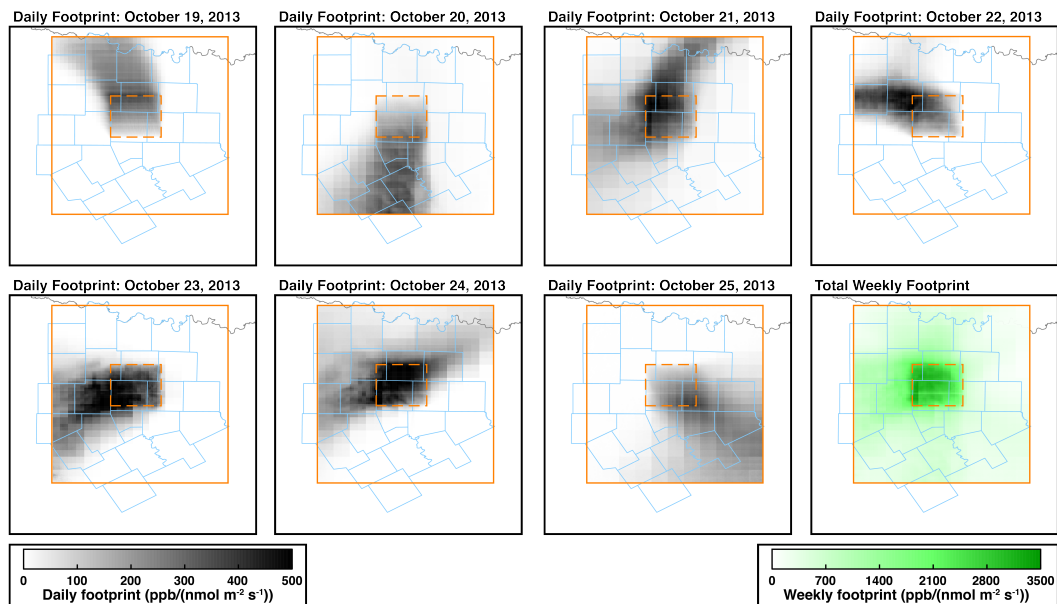


Fig. 2. Summed methane column footprints for all $1.3 \times 1.3 \text{ km}^2$ grid cells in the $70 \times 70 \text{ km}^2$ observation domain defined by the dashed orange box. The footprints are calculated from 8 to 17 local time over the $290 \times 235 \text{ km}^2$ domain defined by the solid orange box. Bottom right panel shows the summed footprint for the full week.

113 Figure 2 shows the sum of all column footprints produced on individual days for the $70 \times 70 \text{ km}^2$
 114 observation domain. Computing these high-resolution footprints was a non-trivial computational
 115 task and ultimately yielded more than 4 Tb of footprints for the week of pseudo-satellite observations
 116 in the Barnett Shale. The footprints show large variability from day to day over the course of the
 117 week, reflecting meteorological variability. For example, winds are from the north on October 19th
 118 and from the south on October 20th. The winds are weak on October 24th, resulting in a strong
 119 local contribution to the footprint. Summing the footprints over the course of the week (bottom right
 120 panel of Fig. 2), we find that the observations are mainly sensitive to the core $70 \times 70 \text{ km}^2$
 121 where they are made, with a diffuse sensitivity over the outer $290 \times 235 \text{ km}^2$ domain. Additional
 122 observations within the outer domain would need to be considered to constrain emissions in that
 123 domain. On the other hand, information on emissions in the $70 \times 70 \text{ km}^2$ core domain is mainly
 124 contributed by observations within the domain. Thus our focus will be to determine the capability of
 125 the observations in the $70 \times 70 \text{ km}^2$ domain to constrain emissions within that same domain, but we
 126 include the outer $290 \times 235 \text{ km}^2$ domain in our footprint analysis for completeness in accounting of

127 information. Previous work from (Turner et al., 2016b, Supplemental Section 6.1) investigated the
128 impact of domain size on error reduction for WRF-STILT inversions in California's Bay Area and
129 found that it had a negligible impact

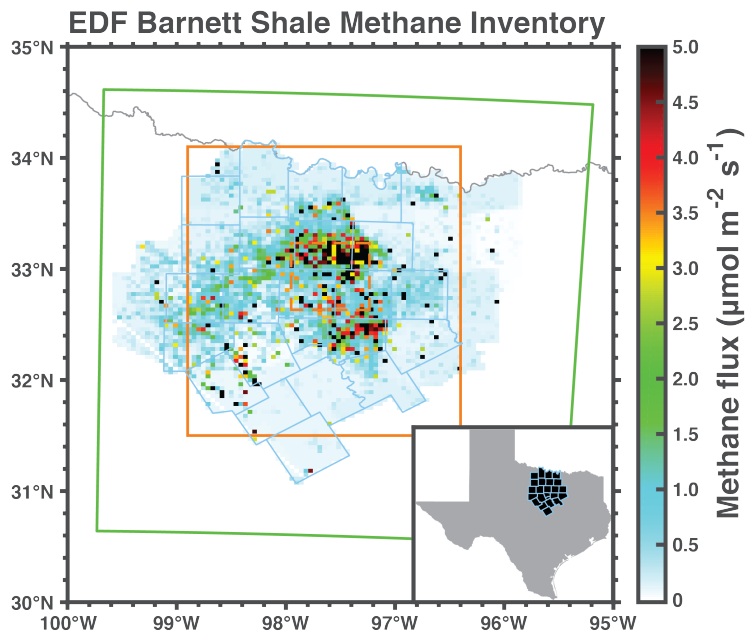


Fig. 3. Gridded Environmental Defense Fund (EDF) methane emission inventory for the Barnett Shale in Texas in October 2013 (Lyon et al., 2015). Spatial resolution is $4 \times 4 \text{ km}^2$. White areas are outside the inventory domain.

130 The footprint information can be combined with an emission inventory for the $290 \times 235 \text{ km}^2$
131 domain to generate a field of column concentrations over the $70 \times 70 \text{ km}^2$ domain as would be ob-
132 served from satellite. We use for this purpose the Environmental Defense Fund (EDF) inventory for
133 the Barnett Shale in October 2013 at $4 \times 4 \text{ km}^2$ resolution compiled by Lyon et al. (2015). We down-
134 scale the EDF inventory by uniform attribution from $4 \times 4 \text{ km}^2$ to $1.3 \times 1.3 \text{ km}^2$ spatial resolution.
135 The inventory is shown in Fig. 3 and includes contributions from oil/gas production, livestock op-
136 erations, landfills, and urban emissions from the Dallas-Fort Worth area. It provides mean monthly
137 values with no temporal resolution, but presumes that some sources will behave as sporadic large
138 transients (Zavala-Araiza et al., 2015). Figure 4 shows an example of the methane column enhance-
139 ments above background (H_x) computed at 9 local time on October 23. We find enhancements
140 in the range of 0-10 ppb due to emissions within the $290 \times 235 \text{ km}^2$ OSSE footprint domain. In
141 what follows we will examine the potential of different satellite observing systems to detect these
142 enhancements relative to the background and interpret them in terms of local sources.

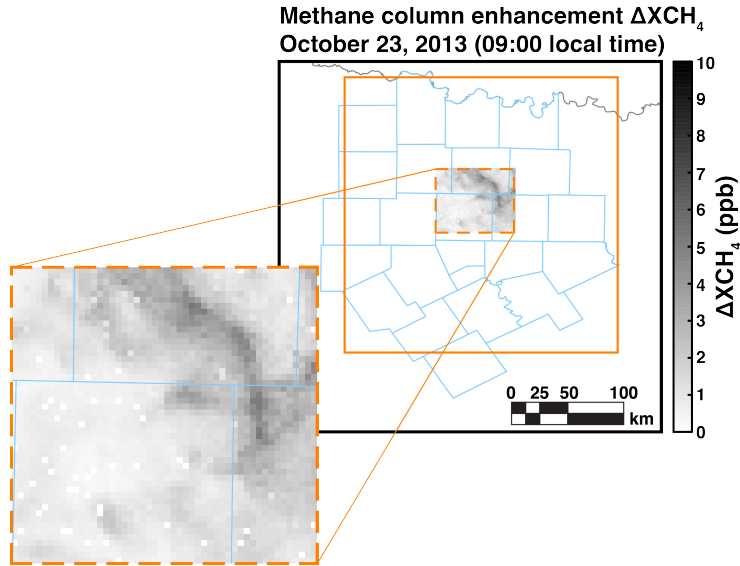


Fig. 4. Simulated methane concentration enhancements relative to background ($\Delta XCH_4 = \mathbf{H}\mathbf{x}$) in the 70×70 km² observation domain of the Barnett Shale (dashed orange box), as derived from the downscaled EDF methane inventory (\mathbf{x}) and the WRF-STILT footprints (\mathbf{H}) within the 290×235 km² OSSE domain (solid orange box). Values are for October 23 at 9 local time. Zeros are due to missing data because of unfinished computations.

Table 1. Satellite observing systems considered in this work.

Instrument	Observation Frequency ^a	Pixel resolution (km ²)	Precision (ppb)
hi-res ^b	hourly	1.3×1.3	1.0
GeoCARB (hourly)	hourly	2.7×3.0	4.0
GeoCARB	twice daily	2.7×3.0	4.0
GeoCARB (daily)	daily	2.7×3.0	4.0
TROPOMI	daily	7.0×7.0	10.8

^aHourly observations are 10 times per day at 8-17 local time, twice daily observations are at 10 and 14 local time, and daily observations are at 13 local time.

^bAspirational instrument with the highest observation frequency and pixel resolution that can be simulated within our OSSE framework.

143 3 Information content of different satellite observing systems

144 We aim to determine the information content from different satellite-based observing systems regard-
145 ing the spatial and temporal distribution of emissions in the Barnett Shale. We consider both steady
146 and potentially transient emissions with 5 different satellite observing configurations (Table 1).
147 TROPOMI (global daily mapping, 7×7 km² nadir pixel resolution, 11 ppb precision; Veefkind et al.,
148 2012) was launched in October 2017 and is expected to provide an operational data stream by the end
149 of 2018. GeoCARB (geostationary, 2.7×3.0 km² pixel resolution, 4 ppb precision; O’Brien et al.,
150 2016) is planned for launch in the early 2020s and its observation schedule is still under discussion
151 with a tentative design for observations twice daily; here we examine different return frequencies of
152 hourly, twice daily, and daily. Finally, the hypothetical “hi-res” configuration assumes geostation-
153 ary hourly observations at the 1.3×1.3 km² pixel resolution of our WRF simulation and with 1 ppb
154 precision; it represents an aspirational system that combines the frequent return time, fine pixel res-
155 olution, and high precision of instruments presently at the proposal stage (Bovensmann et al., 2010;
156 Fishman et al., 2012; Xi et al., 2015). All configurations are filtered for cloudy scenes.

157 The various satellite observing configurations of Table 1 differ in their return frequency, pixel
158 resolution, and instrument precision. The benefit of improving any of these attributes may be lim-
159 ited by error in the forward model used in the inverse analysis (i.e., the Jacobian matrix \mathbf{H}) and by
160 spatial or temporal correlation of the errors. These limitations are described by the model-data mis-
161 match error covariance matrix (\mathbf{R}) including summed contributions from the instrument, forward
162 model, and representation errors (Turner and Jacob, 2015; Brasseur and Jacob, 2017). Represent-
163 ation errors are negligible here because the instrument pixels are commensurate or coarser than
164 the model grid resolution. Instrument error (i.e., precision) is listed in Table 1. Forward model
165 error is estimated by computing STILT footprints for a subset of the meteorological period using
166 the Global Data Assimilation System (GDAS; [https://www.ncdc.noaa.gov/data-access/model-data/
167 model-datasets/global-data-assimilation-system-gdas](https://www.ncdc.noaa.gov/data-access/model-data/model-datasets/global-data-assimilation-system-gdas)), applying the two sets of footprints to either
168 the EDF methane inventory (Fig. 3; Lyon et al., 2015) or the gridded EPA inventory (Maasackers
169 et al., 2016), and computing semivariograms of differences in column concentrations. From this we
170 obtain a forward model error standard deviation of 4 ppb with an error correlation length scale of 40
171 km. We assume a temporal model error correlation length of 2 hours. Sheng et al. (2018b) previ-
172 ously derived a temporal model error correlation length of 5 hours in simulation of TCCON methane
173 column observations at 25 km resolution, and we expect our correlation length to be shorter because
174 of the finer resolution.

175 Bayesian inference is commonly used when estimating methane emissions with atmospheric ob-
176 servations, allowing for errors in the observations and in the prior estimates:

$$P(\mathbf{x}|\mathbf{y}) \propto P(\mathbf{y}|\mathbf{x})P(\mathbf{x}) \quad (3)$$

177 where $P(\mathbf{x}|\mathbf{y})$ is the posterior probability density function (pdf) of the state vector (\mathbf{x}) given the
 178 observations (\mathbf{y}), $P(\mathbf{y}|\mathbf{x})$ is the conditional pdf of \mathbf{y} given \mathbf{x} , and $P(\mathbf{x})$ is the prior pdf of \mathbf{x} . A
 179 common assumption is that $P(\mathbf{y}|\mathbf{x})$ and $P(\mathbf{x})$ are normally distributed which allows us to write the
 180 posterior pdf as

$$P(\mathbf{x}|\mathbf{y}) \propto \exp \left\{ -\frac{1}{2}(\mathbf{y} - \mathbf{H}\mathbf{x})^T \mathbf{R}^{-1}(\mathbf{y} - \mathbf{H}\mathbf{x}) - \frac{1}{2}(\mathbf{x} - \mathbf{x}_a)^T \mathbf{B}^{-1}(\mathbf{x} - \mathbf{x}_a) \right\} \quad (4)$$

181 where \mathbf{B} is the $n \times n$ prior error covariance matrix and \mathbf{x}_a is the $n \times 1$ vector of prior fluxes. The
 182 most probable solution is obtained by minimizing the cost function:

$$\mathcal{J}(\mathbf{x}) = \frac{1}{2}(\mathbf{y} - \mathbf{H}\mathbf{x})^T \mathbf{R}^{-1}(\mathbf{y} - \mathbf{H}\mathbf{x}) + \frac{1}{2}(\mathbf{x} - \mathbf{x}_a)^T \mathbf{B}^{-1}(\mathbf{x} - \mathbf{x}_a) \quad (5)$$

183 yielding the posterior estimate ($\hat{\mathbf{x}}$):

$$\hat{\mathbf{x}} = \mathbf{x}_a + \underbrace{(\mathbf{H}^T \mathbf{R}^{-1} \mathbf{H} + \mathbf{B}^{-1})^{-1}}_{\text{posterior covariance matrix}} \mathbf{H}^T \mathbf{R}^{-1}(\mathbf{y} - \mathbf{H}\mathbf{x}) \quad (6)$$

184 with an $n \times n$ posterior error covariance matrix:

$$\mathbf{Q} = \underbrace{(\mathbf{H}^T \mathbf{R}^{-1} \mathbf{H})}_{\text{observations}} + \underbrace{\mathbf{B}^{-1}}_{\text{prior}} \quad (7)$$

185 that characterizes the uncertainty in the solution. The first term in the posterior covariance ma-
 186 trix is known as the Fisher information matrix: $\mathcal{F} = \mathbf{H}^T \mathbf{R}^{-1} \mathbf{H}$ (see, for example, Rodgers, 2000;
 187 Tarantola, 2004). \mathcal{F} defines the observational contribution to the posterior uncertainty.

188 Comparison between \mathcal{F} and \mathbf{B}^{-1} identifies the extent to which the observations reduce the un-
 189 certainty in the fluxes. Specifically, the number of pieces of information on emissions acquired to
 190 better than measurement error is the number of eigenvalues of $\mathbf{B}^{1/2} \mathcal{F} \mathbf{B}^{1/2}$ that are greater than
 191 unity (Rodgers, 2000). As such, the Fisher information matrix and prior error covariance matrix can
 192 quantify the effective rank of the observing system.

193 A drawback with this formulation of the information content is that it relies on the assumption of
 194 a Gaussian prior pdf. A number of papers have suggested that the pdf of methane emissions from a
 195 given source may be skewed, with a “fat tail” of transient high emissions (e.g., Brandt et al., 2014;
 196 Zavala-Araiza et al., 2015; Frankenberg et al., 2016). Alternate formulations for the cost function
 197 to be minimized may include no prior information (least-squares regression), a prior constraint that
 198 promotes a sparse solution (e.g., Candes and Wakin, 2008), a prior constraint based on frequen-
 199 tist regularization approaches (such as LASSO regression or Tikhonov regularization), or a prior
 200 constraint based on the spatial patterns of emissions rather than their magnitudes (geostatistical in-
 201 version). Table 2 lists the corresponding formulations. From Table 2 we see that the observation term
 202 is the same in all cases. Thus the Fisher information matrix provides a general measure of the in-

Table 2. Cost functions for different formulations of the inverse problem^a.

Method	Cost function
Least-squares regression	$(\mathbf{y} - \mathbf{H}\mathbf{x})^T \mathbf{R}^{-1} (\mathbf{y} - \mathbf{H}\mathbf{x})$
LASSO regression	$(\mathbf{y} - \mathbf{H}\mathbf{x})^T \mathbf{R}^{-1} (\mathbf{y} - \mathbf{H}\mathbf{x}) + \gamma \sum_i x_i $
Tikhonov regularization	$(\mathbf{y} - \mathbf{H}\mathbf{x})^T \mathbf{R}^{-1} (\mathbf{y} - \mathbf{H}\mathbf{x}) + \gamma \mathbf{x}^T \mathbf{x}$
Bayesian inference, Gaussian	$(\mathbf{y} - \mathbf{H}\mathbf{x})^T \mathbf{R}^{-1} (\mathbf{y} - \mathbf{H}\mathbf{x}) + (\mathbf{x} - \mathbf{x}_a)^T \mathbf{B}^{-1} (\mathbf{x} - \mathbf{x}_a)$
Geostatistical inverse model	$(\mathbf{y} - \mathbf{H}\mathbf{x})^T \mathbf{R}^{-1} (\mathbf{y} - \mathbf{H}\mathbf{x}) + (\mathbf{x} - \mathbf{G}\boldsymbol{\beta})^T \mathbf{B}^{-1} (\mathbf{x} - \mathbf{G}\boldsymbol{\beta})$

^a γ is the regularization parameter for LASSO regression and Tikhonov regularization. \mathbf{G} is a matrix with columns corresponding to different spatial datasets and $\boldsymbol{\beta}$ is a vector of drift coefficients for the spatial datasets. Other variables defined in the text.

203 formation content provided by an observing system, independent of the form of the prior constraint,
 204 and we use it in what follows as a measure of the information content.

205 The Fisher information matrix is an $n \times n$ matrix. Each of its n eigenvectors represent an inde-
 206 pendent normalized emission flux pattern and the corresponding eigenvalues are the inverses of the
 207 error variances associated with that pattern. A more useful way of stating this is that the inverse
 208 square root of the i^{th} eigenvalue of \mathcal{F} represents the flux threshold f_i needed for the observations
 209 to be able to constrain the emission flux pattern represented by the i^{th} eigenvector. Whether that
 210 flux threshold is useful depends on the magnitude of the emissions, and this can be assessed for the
 211 problem at hand. Thus the eigenanalysis of the Fisher information matrix gives us a general estimate
 212 of the capability of an observing system to quantify emissions, which can then be applied to any
 213 actual $n \times n$ emission field.

214 For a given emission field, we may expect that some of the n emission flux patterns will be
 215 usefully constrained by the observing system while others are not. The number of patterns that are
 216 usefully constrained represents the number $\mathcal{I} \leq n$ pieces of information on emissions provided by
 217 the observing system. We will equivalently refer to it as the rank of the Fisher information matrix.
 218 This is determined by comparing the eigenvalues of an emission inventory (e_i) to the flux thresholds.
 219 The number of e_i larger than the corresponding f_i provides a cut-off to estimate \mathcal{I} :

$$\mathcal{I} = \sum_i \begin{cases} 1, & e_i > f_i \\ 0, & e_i \leq f_i \end{cases} \quad (8)$$

220 In the case of Bayesian inference, this is roughly equivalent to the degrees of freedom for signal with
 221 a diagonal prior error covariance matrix and a relative uncertainty of 100%. But the eigenanalysis
 222 of the Fisher information matrix provides a more general approach of the capability of an observ-
 223 ing system that can be confronted to any prior constraint and allows intercomparison of different
 224 observing system configurations.

225 There is an inconsistency in this formulation of \mathcal{I} : \mathcal{F} and \mathbf{B}^{-1} have different eigenspaces. In this
 226 work we have chosen to treat these matrices separately because, in practice, it is computationally

227 infeasible to directly compute the eigenvalues of the matrix product if n is large, as in the case here
228 of constraining hourly emissions of the spatially distributed inventory. This inconsistency results in
229 our estimate of \mathcal{I} likely being an upper bound on the information content (see Appendix for details).

230 **4 Comparing different satellite configurations**

231 The eigenanalysis of Section 3 allows us to intercompare the value of different satellite configura-
232 tions for resolving the fine-scale patterns of methane emissions within a given domain. Here we
233 apply it to the Barnett Shale domain of Section 2. We consider two limiting cases: Case #1 assumes
234 the emissions to be temporally invariant and Case #2 assumes the emissions to vary hourly with no
235 temporal correlation. In Case #1 the problem is typically overdetermined ($m > n$), depending on
236 the satellite configuration, and the maximum rank of \mathcal{F} is n (the number of emission grid cells). In
237 Case #2 the problem is underdetermined ($m < n$) and the maximum rank of \mathcal{F} is m (the number of
238 observations).

239 In both Case #1 and #2, the observations only provide useful information (as defined by Eq. 8) if
240 the signal is larger than the noise, as diagnosed by the $e_i > f_i$ criterion of Eq. 8. Here the emissions
241 are the downscaled EDF inventory, which includes 40,140 grid cells in the 290×235 km² inversion
242 domain ($n = 40,140$ in Case #1 with temporally invariant emissions) but only 2,601 of those grid
243 cells are within the 70×70 km² observation domain (dashed orange box in Fig. 1) where we might
244 expect the observations to provide the strongest constraints. In Case #2 with temporally variable
245 emissions we have $n = 40,140 \times 24 = 963,360$ grid cells for a single day.

246 Figure 5 shows the ensemble of flux thresholds for the five satellite configurations, assuming
247 temporally invariant emissions. The ranked flux patterns are on the abscissa; leading flux patterns
248 correspond to larger patterns of variability (e.g., regional-scale emissions), and the trailing flux pat-
249 terns correspond to fine-scale variability. The corresponding flux thresholds are on the ordinate.
250 The flux threshold is lowest for the leading flux patterns and largest for the trailing flux patterns.
251 This means that the regional-scale emissions are easiest to quantify and the finer-scale emissions are
252 increasingly difficult to quantify. The information content (\mathcal{I}) is obtained from the intersection of
253 the flux thresholds (colored lines) with the eigenvalues from the emission inventory (black line). A
254 higher information content means that finer scales of emission variability can be detected.

255 From Fig. 5, we see that a week of TROPOMI observations provides 5 pieces of information on
256 emissions for the 70×70 km² core domain out of a possible 2601 pieces of information describing
257 the emissions on the 1.3×1.3 km² grid. The actual pieces of information are the eigenvectors of the
258 Fisher information matrix, and the ranked eigenvectors describe gradually finer patterns of variability
259 from 70×70 to 1.3×1.3 km². The k^{th} ranked eigenvector may be assumed to describe an emission
260 pattern of dimension $70/\sqrt{k}$, implying that TROPOMI can resolve emissions on a 30 km scale.

261 The three GeoCARB configurations provide 98–961 pieces of information dependent on whether

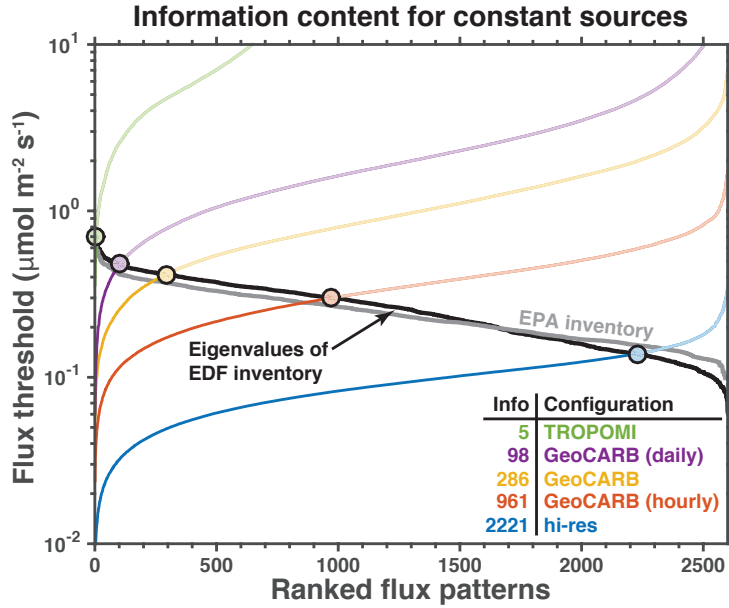


Fig. 5. Capability of different configurations for satellite observations of atmospheric methane (Table 1) to resolve the fine-scale ($1.3 \times 1.3 \text{ km}^2$) patterns of variability of temporally invariant emissions in a $290 \times 235 \text{ km}^2$ domain and for a 1-week observation period. The colored lines show the flux thresholds for the different emission patterns of variability in the domain, as given by the ordered inverse square roots of the eigenvalues of the Fisher information matrix. Solid black line is the eigenvalues of the emissions from the EDF Barnett Shale methane inventory (Lyon et al., 2015) and the solid gray line is the gridded EPA inventory. The region above the black line is where the noise is larger than the signal. Filled circles indicate the information content of the observing system (\mathcal{I}) for a given satellite configuration at $1.3 \times 1.3 \text{ km}^2$ spatial resolution. Inset table lists the information contents for the five configurations.

262 the observations are daily, twice daily, or hourly. Following the above assumption, this corresponds
 263 to resolving emissions on a $\sim 2\text{-}7 \text{ km}$ scale. Hourly observations provide 10 times more information
 264 (as defined by Eq. 8) on emission patterns than daily observations, and 3 times more than twice-daily
 265 observations (the default configuration of GeoCARB). Remarkably, more is gained by going from
 266 daily to twice-daily (factor of 3.4) than going from twice-daily to hourly (factor of 2.9), because of
 267 the temporal error correlation in the transport model. The aspirational hi-res satellite configuration
 268 provides 2,221 pieces of information on temporally invariant sources, corresponding to 85% of the
 269 flux patterns in the $70 \times 70 \text{ km}^2$ observation region, which means that much of the spatial variability
 270 in the $1.3 \times 1.3 \text{ km}^2$ emissions in the Barnett Shale is resolved.

271 Figure 6 further quantifies the importance of instrument precision and return frequency for the
 272 GeoCARB pixel resolution of $2.7 \times 3.0 \text{ km}^2$. It shows the flux thresholds for a set of configurations
 273 where the instrument precision is varied from 0 to 14 ppb and the return frequency is varied from 1
 274 to 10 returns per day. We find that instrument precision is more important than return frequency for

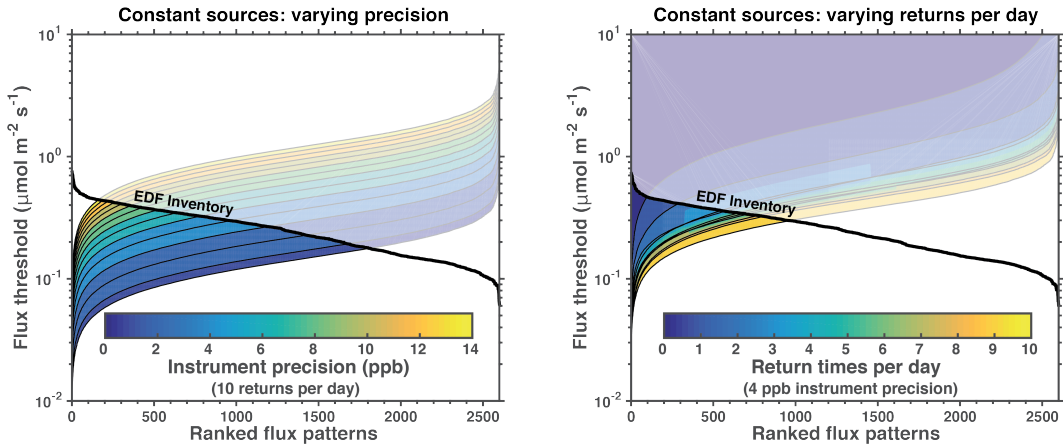


Fig. 6. Capability of GeoCARB-like satellite configurations to resolve the fine-scale ($1.3 \times 1.3 \text{ km}^2$) patterns of variability of temporally invariant emissions in a $290 \times 235 \text{ km}^2$ domain and for a 1-week observation period. Left panel shows the results for a configuration with 10 returns per day (hourly observations) where the instrument precision is varied from 0 to 14 ppb. Right panel shows the results for a configuration with 4 ppb instrument precision and the return frequency per day is varied from 1 to 10. Solid black line shows eigenvalues of the EDF Barnett Shale methane emission inventory (Lyon et al., 2015). The region above the black line is where the noise is larger than the signal. The change in flux threshold as the sampling frequency increases in the right panel is not necessarily monotonic, this is because some of the cases use different subsets of observation (e.g., daily observations are at 13 local time while twice daily are at 10 and 14).

275 increasing the information content from the observations.

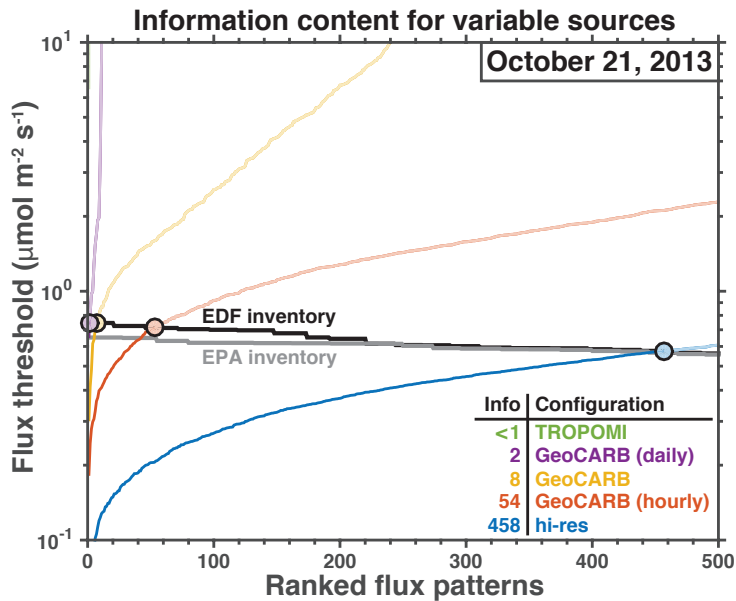


Fig. 7. Same as Fig. 5 but for temporally variable sources on October 21, 2013.

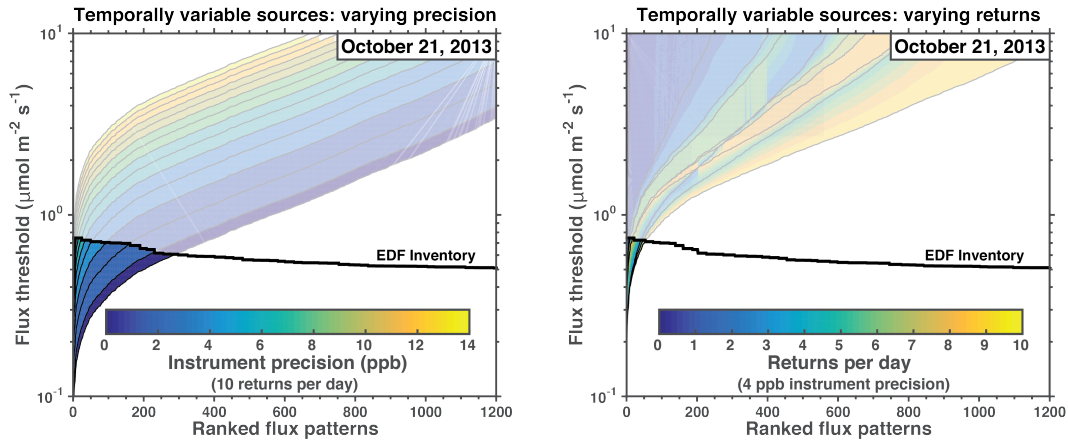


Fig. 8. Same as Fig. 6 but for temporally variable sources on October 21, 2013.

276 In Case #2 we assume that the methane sources in individual pixels vary in time on an hourly
 277 basis with no correlation from one hour to the next, making the problem generally underdetermined
 278 ($m < n$) for all satellite configurations. Here we aim to determine the ability of the satellite obser-
 279 vations to quantify the hourly emissions over the spatial patterns defined by the eigenvectors of \mathcal{F}
 280 and making no assumption as to the persistence of those emissions. We treat each day independently
 281 and compute the eigenvalues of the Fisher information matrix for each day. Figure 7 shows the
 282 flux thresholds for the five satellite configurations on a representative day. From Fig. 7, we see that
 283 TROPOMI is unable to provide any information on hourly emissions in the Barnett Shale. The three
 284 GeoCARB configurations provide 2–54 pieces of information. Fig. 8 evaluates the impact of sam-
 285 pling frequency and instrument precision for the GeoCARB configurations. As with the temporally
 286 invariant case, we find that instrument precision is more important for increasing the information
 287 content. The aspirational “hi-res” configuration (shown in Fig. 7) is the only configuration that is
 288 able to provide substantial information (458 pieces of information) on temporally variable emissions.

289 Figure 9 summarizes the findings from Figs. 6 and 8. It compares the information content \mathcal{I}
 290 from configurations with $2.7 \times 3.0 \text{ km}^2$ spatial resolution (GeoCARB) as the instrument precision
 291 and return frequency are varied from 0 to 14 ppb and 1 to 10 returns per day, respectively, for both
 292 temporally variable and constant sources. Uncertainty on \mathcal{I} is estimated by randomly sampling e_i
 293 from the ensemble of emission inventory eigenvalues and comparing to f_i in Eq. 8. For the tempo-
 294 rally invariant sources (Case #1), we find considerable increases in information content for instru-
 295 ment precisions better than 6 ppb (top left panel in Fig. 9) and an approximately linear relationship
 296 between information content and return frequency (top right panel in Fig. 9). The satellite configu-
 297 rations provide considerably less information for the temporally variable sources (Case #2). We find
 298 that satellite configurations with instrument precision worse than 6 ppb provide no information on
 299 temporally variable sources (bottom left panel in Fig. 9). As with the temporally invariant case, we
 300 find an approximately linear relationship between information content and return frequency (bottom

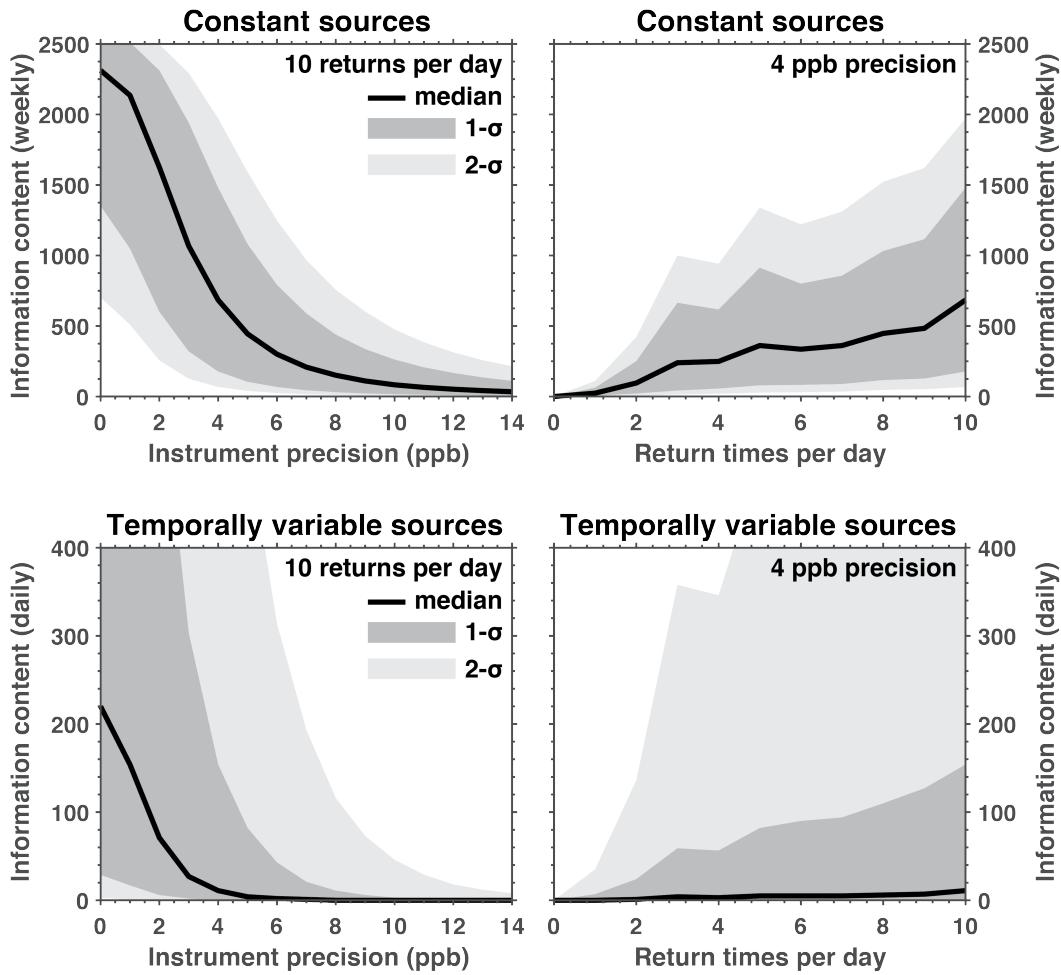


Fig. 9. Information content \mathcal{I} as a function of the instrument precision (left column) and the sampling frequency per day (right column) for a satellite with a pixel resolution of $2.7 \times 3.0 \text{ km}^2$. Top row is for Case #1 where the sources are assumed to be temporally invariant and bottom row is for Case #2 where the sources are temporally variable. Solid black line is the median information content. A 4 ppb model error is included, see Section 3. Uncertainty is from randomly sampling e_i from the eigenvalues of the EDF inventory.

301 right panel in Fig. 9). From this, we conclude that a GeoCARB-like instrument would greatly benefit
302 from having an instrument precision better than 6 ppb.

303 5 Conclusions

304 We conducted an observing system simulation experiment (OSSE) to evaluate the potential of dif-
305 ferent satellite observation systems for atmospheric methane to quantify methane emissions at kilo-
306 meter scale. This involved a 1-week WRF-STILT simulation of atmospheric methane columns with
307 $1.3 \times 1.3 \text{ km}^2$ spatial resolution over the $290 \times 235 \text{ km}^2$ Barnett Shale domain to quantify the in-
308 formation content of different satellite instrument configurations for resolving the kilometer-scale
309 distribution of methane emissions within that domain. We evaluated the information content of the
310 different satellite observing systems through an eigenanalysis of the Fisher information matrix \mathcal{F} ,
311 which characterizes the capability of an observing system independently of the form of the prior
312 information. The eigenvalues of \mathcal{F} define the emission flux thresholds for detection of emission
313 patterns down to 1.3 km in scale as defined by the eigenvectors. Here we put these flux thresholds in
314 context of the high-resolution EDF emission inventory for the Barnett Shale to quantify the informa-
315 tion content from different satellite observing configurations. The same approach could be readily
316 used for different observation domains and different prior inventories.

317 We find from this analysis that the recently launched TROPOMI satellite instrument (low Earth
318 orbit, $7 \times 7 \text{ km}^2$ pixels, daily return time, 11 ppb precision) should be able to constrain the mean
319 emissions in the Barnett Shale and provide some coarse-resolution information on the distribution of
320 temporally invariant emissions at $\sim 30 \text{ km}$ scales. The planned GeoCARB instrument (geostationary
321 orbit, $2.7 \times 3.0 \text{ km}^2$ pixels, twice-daily return time, 4 ppb precision), will provide 50 times more
322 information than TROPOMI. The observing frequency of GeoCARB is still under discussion; we
323 find that twice-daily observations triple the information content relative to daily observations, while
324 hourly observations allow another tripling. The 4 ppb precision of GeoCARB is well adapted to
325 the magnitude of methane sources; we find that a precision larger than 6 ppb would considerably
326 decrease the information content. An aspirational “hi-res” instrument using attributes of currently
327 proposed instruments (geostationary orbit, $1.3 \times 1.3 \text{ km}^2$ pixels, hourly return time, 1 ppb precision)
328 can resolve much of the kilometer-scale spatial distribution in the EDF inventory. This assumes
329 that the emissions are constant in time or that their temporal variability is known. Resolving hourly
330 variable emissions at the kilometer-scale will be very limited even with the aspirational “hi-res”
331 instrument.

332 Appendix Computing the information content

333 We treat \mathcal{F} and \mathbf{B}^{-1} separately because it is computationally infeasible to compute the eigenval-
334 ues of the matrix product when we attempt to resolve hourly emissions as $n > 10^6$ and both \mathcal{F}

335 and \mathbf{B}^{-1} are $n \times n$ matrices. This separation of \mathcal{F} and \mathbf{B}^{-1} results in our estimate of \mathcal{I} likely be-
 336 ing an upper bound on the information content. This follows from Bhatia (1997) who prove that
 337 $\lambda(\mathbf{CD}) \prec_w \lambda^\downarrow(\mathbf{C}) \cdot \lambda^\downarrow(\mathbf{D})$, where \mathbf{C} and \mathbf{D} are Hermitian positive definite matrices, $\lambda^\downarrow(\mathbf{X})$ de-
 338 notes the vector of eigenvalues of \mathbf{X} in decreasing order, \prec_w is the weak majorization preorder,
 339 and $\mathbf{p} \cdot \mathbf{q} = (p_1 q_1, \dots, p_n q_n)$. Therefore, directly computing the eigenvalues of $\mathbf{B}^{1/2} \mathcal{F} \mathbf{B}^{1/2}$, as
 340 Rodgers (2000) suggests for the Bayesian inference case with Gaussian errors, would likely yield
 341 fewer eigenvalues larger than unity than our estimate.

342 In the case of temporally variable emissions, the system is generally underdetermined ($m < n$) and
 343 we can use a singular value decomposition to efficiently compute the eigenvalues of \mathcal{F} . For an $m \times n$
 344 real matrix \mathbf{A} , the non-zero singular values of $\mathbf{A}^T \mathbf{A}$ and $\mathbf{A} \mathbf{A}^T$ are identical even though the singular
 345 vectors are different (see, for example, Rodgers, 2000) but the dimensions of these two matrices are
 346 $n \times n$ and $m \times m$, respectively, and the eigenvalues can be computed from the square root of the
 347 non-zero singular values. We can write $\mathcal{F} = \hat{\mathbf{H}}^T \hat{\mathbf{H}}$ where $\hat{\mathbf{H}} = \mathbf{L}^{-1} \mathbf{H}$ is the pre-whitened Jacobian
 348 and \mathbf{L} is a lower triangular matrix from a Cholesky decomposition of \mathbf{R} (such that $\mathbf{R} = \mathbf{L} \mathbf{L}^T$). Thus,
 349 the eigenvalues of \mathcal{F} can be obtained by analysis of either $\hat{\mathbf{H}}^T \hat{\mathbf{H}}$ (an $n \times n$ matrix) or $\hat{\mathbf{H}} \hat{\mathbf{H}}^T$ (an
 350 $m \times m$ matrix).

351 *Acknowledgements.* This work was supported by the ExxonMobil Research and Engineering Company and
 352 the US Department of Energy (DOE) Advanced Research Projects Agency – Energy (ARPA-E). A. J. Turner
 353 is supported as a Miller Fellow with the Miller Institute for Basic Research in Science at UC Berkeley. This
 354 research used the Savio computational cluster resource provided by the Berkeley Research Computing program
 355 at the University of California, Berkeley (supported by the UC Berkeley Chancellor, Vice Chancellor for Re-
 356 search, and Chief Information Officer). This research also used resources from the National Energy Research
 357 Scientific Computing Center, which is supported by the Office of Science of the U.S. Department of Energy
 358 under Contract No. DE-AC02-05CH11231. We also acknowledge high-performance computing support from
 359 Cheyenne (doi:10.5065/D6RX99HX) provided by NCAR’s Computational and Information Systems Labora-
 360 tory, sponsored by the National Science Foundation.

361 References

- 362 Alexe, M., Bergamaschi, P., Segers, A., Detmers, R., Butz, A., Hasekamp, O., Guerlet, S., Parker, R., Boesch,
363 H., Frankenberg, C., Scheepmaker, R. A., Dlugokencky, E., Sweeney, C., Wofsy, S. C., and Kort, E. A.:
364 Inverse modelling of CH₄ emissions for 2010–2011 using different satellite retrieval products from GOSAT
365 and SCIAMACHY, *Atmospheric Chemistry and Physics*, 15, 113–133, doi:10.5194/acp-15-113-2015, 2015.
- 366 Bergamaschi, P., Frankenberg, C., Meirink, J. F., Krol, M., Villani, M. G., Houweling, S., Dentener, F., Dlu-
367 gokencky, E. J., Miller, J. B., Gatti, L. V., Engel, A., and Levin, I.: Inverse modeling of global and re-
368 gional CH₄ emissions using SCIAMACHY satellite retrievals, *Journal of Geophysical Research*, 114, doi:
369 10.1029/2009jd012287, 2009.
- 370 Bergamaschi, P., Houweling, S., Segers, A., Krol, M., Frankenberg, C., Scheepmaker, R. A., Dlugokencky, E.,
371 Wofsy, S. C., Kort, E. A., Sweeney, C., Schuck, T., Brenninkmeijer, C., Chen, H., Beck, V., and Gerbig, C.:
372 Atmospheric CH₄ in the first decade of the 21st century: Inverse modeling analysis using SCIAMACHY
373 satellite retrievals and NOAA surface measurements, *Journal of Geophysical Research: Atmospheres*, 118,
374 7350–7369, doi:10.1002/jgrd.50480, 2013.
- 375 Bhatia, R.: *Matrix Analysis*, Graduate Texts in Mathematics, Springer, New York, 1997.
- 376 Bousserez, N., Henze, D. K., Rooney, B., Perkins, A., Wecht, K. J., Turner, A. J., Natraj, V., and Worden,
377 J. R.: Constraints on methane emissions in North America from future geostationary remote-sensing mea-
378 surements, *Atmospheric Chemistry and Physics*, 16, 6175–6190, doi:10.5194/acp-16-6175-2016, 2016.
- 379 Bovensmann, H., Buchwitz, M., Burrows, J. P., Reuter, M., Krings, T., Gerilowski, K., Schneising, O., Hey-
380 mann, J., Tretner, A., and Erzinger, J.: A remote sensing technique for global monitoring of power plant
381 CO₂ emissions from space and related applications, *Atmospheric Measurement Techniques*, 3, 781–811,
382 doi:10.5194/amt-3-781-2010, 2010.
- 383 Brandt, A. R., Heath, G. A., Kort, E. A., O’Sullivan, F., Petron, G., Jordaan, S. M., Tans, P., Wilcox, J.,
384 Gopstein, A. M., Arent, D., Wofsy, S., Brown, N. J., Bradley, R., Stucky, G. D., Eardley, D., and Harriss,
385 R.: Energy and environment. Methane leaks from North American natural gas systems, *Science*, 343, 733–5,
386 doi:10.1126/science.1247045, 2014.
- 387 Brasseur, G. P. and Jacob, D. J.: *Modeling of Atmospheric Chemistry*, Princeton University Press, Princeton,
388 NJ, 2017.
- 389 Buchwitz, M., Reuter, M., Schneising, O., Boesch, H., Guerlet, S., Dils, B., Aben, I., Armante, R., Bergamaschi,
390 P., Blumenstock, T., Bovensmann, H., Brunner, D., Buchmann, B., Burrows, J. P., Butz, A., Chdin, A.,
391 Chevallier, F., Crevoisier, C. D., Deutscher, N. M., Frankenberg, C., Hase, F., Hasekamp, O. P., Heymann,
392 J., Kaminski, T., Laeng, A., Lichtenberg, G., De Mazire, M., Nol, S., Notholt, J., Orphal, J., Popp, C.,
393 Parker, R., Scholze, M., Sussmann, R., Stiller, G. P., Warneke, T., Zehner, C., Bril, A., Crisp, D., Griffith,
394 D. W. T., Kuze, A., O’Dell, C., Oshchepkov, S., Sherlock, V., Suto, H., Wennberg, P., Wunch, D., Yokota,
395 T., and Yoshida, Y.: The Greenhouse Gas Climate Change Initiative (GHG-CCI): Comparison and quality
396 assessment of near-surface-sensitive satellite-derived CO₂ and CH₄ global data sets, *Remote Sensing of*
397 *Environment*, 162, 344–362, doi:10.1016/j.rse.2013.04.024, 2015.
- 398 Buchwitz, M., Schneising, O., Reuter, M., Heymann, J., Krautwurst, S., Bovensmann, H., Burrows, J. P.,
399 Boesch, H., Parker, R. J., Somkuti, P., Detmers, R. G., Hasekamp, O. P., Aben, I., Butz, A., Frankenberg,
400 C., and Turner, A. J.: Satellite-derived methane hotspot emission estimates using a fast data-driven method,

401 Atmospheric Chemistry and Physics, 17, 5751–5774, doi:10.5194/acp-17-5751-2017, 2017.

402 Butz, A., Galli, A., Hasekamp, O., Landgraf, J., Tol, P., and Aben, I.: TROPOMI aboard Sentinel-5 Precursor:
403 Prospective performance of CH₄ retrievals for aerosol and cirrus loaded atmospheres, Remote Sensing of
404 Environment, 120, 267–276, doi:10.1016/j.rse.2011.05.030, 2012.

405 Butz, A., Orphal, J., Checa-Garcia, R., Friedl-Vallon, F., von Clarmann, T., Bovensmann, H., Hasekamp, O.,
406 Landgraf, J., Knigge, T., Weise, D., Sqalli-Houssini, O., and Kemper, D.: Geostationary Emission Explorer
407 for Europe (G3E): mission concept and initial performance assessment, Atmospheric Measurement Tech-
408 niques, 8, 4719–4734, doi:10.5194/amt-8-4719-2015, 2015.

409 Candes, E. J. and Wakin, M. B.: An introduction to compressive sampling, IEEE Signal Processing Magazine,
410 25, 21–30, doi:10.1109/Msp.2007.914731, 2008.

411 Caulton, D. R., Shepson, P. B., Santoro, R. L., Sparks, J. P., Howarth, R. W., Ingraffea, A. R., Cambaliza,
412 M. O., Sweeney, C., Karion, A., Davis, K. J., Stirm, B. H., Montzka, S. A., and Miller, B. R.: Toward a
413 better understanding and quantification of methane emissions from shale gas development, Proc Natl Acad
414 Sci U S A, doi:10.1073/pnas.1316546111, 2014.

415 Conley, S., Franco, G., Faloon, I., Blake, D. R., Peischl, J., and Ryerson, T. B.: Methane emissions from
416 the 2015 Aliso Canyon blowout in Los Angeles, CA, Science, 351, 1317–20, doi:10.1126/science.aaf2348,
417 2016.

418 Cressot, C., Chevallier, F., Bousquet, P., Crevoisier, C., Dlugokencky, E. J., Fortems-Cheiney, A., Frankenberg,
419 C., Parker, R., Pison, I., Scheepmaker, R. A., Montzka, S. A., Krummel, P. B., Steele, L. P., and Langenfelds,
420 R. L.: On the consistency between global and regional methane emissions inferred from SCIAMACHY,
421 TANSO-FTS, IASI and surface measurements, Atmospheric Chemistry and Physics, 14, 577–592, doi:10.
422 5194/acp-14-577-2014, 2014.

423 Fishman, J., Iraci, L. T., Al-Saadi, J., Chance, K., Chavez, F., Chin, M., Coble, P., Davis, C., DiGiacomo, P. M.,
424 Edwards, D., Eldering, A., Goes, J., Herman, J., Hu, C., Jacob, D. J., Jordan, C., Kawa, S. R., Key, R., Liu,
425 X., Lohrenz, S., Mannino, A., Natraj, V., Neil, D., Neu, J., Newchurch, M., Pickering, K., Salisbury, J.,
426 Sosik, H., Subramaniam, A., Tzortziou, M., Wang, J., and Wang, M.: The United States’ Next Generation of
427 Atmospheric Composition and Coastal Ecosystem Measurements: NASA’s Geostationary Coastal and Air
428 Pollution Events (GEO-CAPE) Mission, Bulletin of the American Meteorological Society, 93, 1547–1566,
429 doi:10.1175/bams-d-11-00201.1, 2012.

430 Frankenberg, C., Meirink, J. F., van Weele, M., Platt, U., and Wagner, T.: Assessing methane emissions from
431 global space-borne observations, Science, 308, 1010–4, doi:10.1126/science.1106644, 2005.

432 Frankenberg, C., Thorpe, A. K., Thompson, D. R., Hulley, G., Kort, E. A., Vance, N., Borchardt, J., Krings, T.,
433 Gerilowski, K., Sweeney, C., Conley, S., Bue, B. D., Aubrey, A. D., Hook, S., and Green, R. O.: Airborne
434 methane remote measurements reveal heavy-tail flux distribution in Four Corners region, Proc Natl Acad Sci
435 U S A, 113, 9734–9, doi:10.1073/pnas.1605617113, 2016.

436 Fraser, A., Palmer, P. I., Feng, L., Boesch, H., Cogan, A., Parker, R., Dlugokencky, E. J., Fraser, P. J., Krummel,
437 P. B., Langenfelds, R. L., O’Doherty, S., Prinn, R. G., Steele, L. P., van der Schoot, M., and Weiss, R. F.:
438 Estimating regional methane surface fluxes: the relative importance of surface and GOSAT mole fraction
439 measurements, Atmospheric Chemistry and Physics, 13, 5697–5713, doi:10.5194/acp-13-5697-2013, 2013.

440 Houweling, S., Bergamaschi, P., Chevallier, F., Heimann, M., Kaminski, T., Krol, M., Michalak, A. M., and Pa-

441 tra, P.: Global inverse modeling of CH₄ sources and sinks: An overview of methods, *Atmospheric Chemistry*
442 *and Physics Discussions*, pp. 1–30, doi:10.5194/acp-2016-572, 2016.

443 Hu, H., Hasekamp, O., Butz, A., Galli, A., Landgraf, J., Aan de Brugh, J., Borsdorff, T., Scheepmaker, R.,
444 and Aben, I.: The operational methane retrieval algorithm for TROPOMI, *Atmospheric Measurement Tech-*
445 *niques*, 9, 5423–5440, doi:10.5194/amt-9-5423-2016, 2016.

446 Hu, H., Landgraf, J., Detmers, R., Borsdorff, T., Aan de Brugh, J., Aben, I., Butz, A., and Hasekamp, O.:
447 Toward Global Mapping of Methane With TROPOMI: First Results and Intersatellite Comparison to GOSAT,
448 *Geophysical Research Letters*, doi:10.1002/2018gl077259, 2018.

449 Jacob, D. J., Turner, A. J., Maasackers, J. D., Sheng, J., Sun, K., Liu, X., Chance, K., Aben, I., McKeever, J.,
450 and Frankenberg, C.: Satellite observations of atmospheric methane and their value for quantifying methane
451 emissions, *Atmospheric Chemistry and Physics*, 16, 14371–14396, doi:10.5194/acp-16-14371-2016, 2016.

452 Karion, A., Sweeney, C., Ptron, G., Frost, G., Michael Hardesty, R., Kofler, J., Miller, B. R., Newberger, T.,
453 Wolter, S., Banta, R., Brewer, A., Dlugokencky, E., Lang, P., Montzka, S. A., Schnell, R., Tans, P., Trainer,
454 M., Zamora, R., and Conley, S.: Methane emissions estimate from airborne measurements over a western
455 United States natural gas field, *Geophysical Research Letters*, 40, 4393–4397, doi:10.1002/grl.50811, 2013.

456 Karion, A., Sweeney, C., Kort, E. A., Shepson, P. B., Brewer, A., Cambaliza, M., Conley, S. A., Davis, K.,
457 Deng, A., Hardesty, M., Herndon, S. C., Lauvaux, T., Lavoie, T., Lyon, D., Newberger, T., Petron, G., Rella,
458 C., Smith, M., Wolter, S., Yacovitch, T. I., and Tans, P.: Aircraft-Based Estimate of Total Methane Emissions
459 from the Barnett Shale Region, *Environ Sci Technol*, 49, 8124–31, doi:10.1021/acs.est.5b00217, 2015.

460 Kirschke, S., Bousquet, P., Ciais, P., Saunois, M., Canadell, J. G., Dlugokencky, E. J., Bergamaschi, P.,
461 Bergmann, D., Blake, D. R., Bruhwiler, L., Cameron-Smith, P., Castaldi, S., Chevallier, F., Feng, L., Fraser,
462 A., Heimann, M., Hodson, E. L., Houweling, S., Josse, B., Fraser, P. J., Krummel, P. B., Lamarque, J.-F.,
463 Langenfelds, R. L., Le Qur, C., Naik, V., O’Doherty, S., Palmer, P. I., Pison, I., Plummer, D., Poulter, B.,
464 Prinn, R. G., Rigby, M., Ringeval, B., Santini, M., Schmidt, M., Shindell, D. T., Simpson, I. J., Spahni, R.,
465 Steele, L. P., Strode, S. A., Sudo, K., Szopa, S., van der Werf, G. R., Voulgarakis, A., van Weele, M., Weiss,
466 R. F., Williams, J. E., and Zeng, G.: Three decades of global methane sources and sinks, *Nature Geoscience*,
467 6, 813–823, doi:10.1038/ngeo1955, 2013.

468 Kort, E. A., Frankenberg, C., Costigan, K. R., Lindenmaier, R., Dubey, M. K., and Wunch, D.: Four
469 corners: The largest US methane anomaly viewed from space, *Geophysical Research Letters*, 41, doi:
470 10.1002/2014gl061503, 2014.

471 Kuze, A., Suto, H., Nakajima, M., and Hamazaki, T.: Thermal and near infrared sensor for carbon observation
472 Fourier-transform spectrometer on the Greenhouse Gases Observing Satellite for greenhouse gases monitor-
473 ing, *Appl Opt*, 48, 6716–33, doi:10.1364/AO.48.006716, 2009.

474 Kuze, A., Suto, H., Shiomi, K., Kawakami, S., Tanaka, M., Ueda, Y., Deguchi, A., Yoshida, J., Yamamoto,
475 Y., Kataoka, F., Taylor, T. E., and Buijs, H. L.: Update on GOSAT TANSO-FTS performance, operations,
476 and data products after more than 6 years in space, *Atmospheric Measurement Techniques*, 9, 2445–2461,
477 doi:10.5194/amt-9-2445-2016, 2016.

478 Lavoie, T. N., Shepson, P. B., Cambaliza, M. O., Stirm, B. H., Karion, A., Sweeney, C., Yacovitch, T. I.,
479 Herndon, S. C., Lan, X., and Lyon, D.: Aircraft-Based Measurements of Point Source Methane Emissions
480 in the Barnett Shale Basin, *Environ Sci Technol*, 49, 7904–13, doi:10.1021/acs.est.5b00410, 2015.

481 Lin, J. C., Gerbig, C., Wofsy, S. C., Andrews, A. E., Daube, B. C., Davis, K. J., and Grainger, C. A.: A near-
482 field tool for simulating the upstream influence of atmospheric observations: The Stochastic Time-Inverted
483 Lagrangian Transport (STILT) model, *Journal of Geophysical Research-Atmospheres*, 108, ACH 2–1–ACH
484 2–17, doi:10.1029/2002jd003161, 2003.

485 Lyon, D. R., Zavala-Araiza, D., Alvarez, R. A., Harriss, R., Palacios, V., Lan, X., Talbot, R., Lavoie, T.,
486 Shepson, P., Yacovitch, T. I., Herndon, S. C., Marchese, A. J., Zimmerle, D., Robinson, A. L., and Hamburg,
487 S. P.: Constructing a Spatially Resolved Methane Emission Inventory for the Barnett Shale Region, *Environ*
488 *Sci Technol*, 49, 8147–57, doi:10.1021/es506359c, 2015.

489 Maasackers, J. D., Jacob, D. J., Sulprizio, M. P., Turner, A. J., Weitz, M., Wirth, T., Hight, C., DeFigueiredo,
490 M., Desai, M., Schmeltz, R., Hockstad, L., Bloom, A. A., Bowman, K. W., Jeong, S., and Fischer, M. L.:
491 Gridded National Inventory of U.S. Methane Emissions, *Environ Sci Technol*, 50, 13 123–13 133, doi:10.
492 1021/acs.est.6b02878, 2016.

493 Miller, S. M., Wofsy, S. C., Michalak, A. M., Kort, E. A., Andrews, A. E., Biraud, S. C., Dlugokencky,
494 E. J., Eluszkiewicz, J., Fischer, M. L., Janssens-Maenhout, G., Miller, B. R., Miller, J. B., Montzka, S. A.,
495 Nehr Korn, T., and Sweeney, C.: Anthropogenic emissions of methane in the United States, *Proc Natl Acad*
496 *Sci U S A*, 110, 20018–22, doi:10.1073/pnas.1314392110, 2013.

497 Monteil, G., Houweling, S., Butz, A., Guerlet, S., Schepers, D., Hasekamp, O., Frankenberg, C., Scheep-
498 maker, R., Aben, I., and Rckmann, T.: Comparison of CH₄ inversions based on 15 months of GOSAT
499 and SCIAMACHY observations, *Journal of Geophysical Research: Atmospheres*, 118, 11,807–11,823, doi:
500 10.1002/2013jd019760, 2013.

501 O’Brien, D. M., Polonsky, I. N., Utembe, S. R., and Rayner, P. J.: Potential of a geostationary geoCARB
502 mission to estimate surface emissions of CO₂, CH₄ and CO in a polluted urban environment: case study
503 Shanghai, *Atmospheric Measurement Techniques*, 9, 4633–4654, doi:10.5194/amt-9-4633-2016, 2016.

504 O’Dell, C. W., Connor, B., Bsch, H., O’Brien, D., Frankenberg, C., Castano, R., Christi, M., Eldering, D.,
505 Fisher, B., Gunson, M., McDuffie, J., Miller, C. E., Natraj, V., Oyafuso, F., Polonsky, I., Smyth, M., Taylor,
506 T., Toon, G. C., Wennberg, P. O., and Wunch, D.: The ACOS CO₂ retrieval algorithm Part 1: Description
507 and validation against synthetic observations, *Atmospheric Measurement Techniques*, 5, 99–121, doi:10.
508 5194/amt-5-99-2012, 2012.

509 Peischl, J., Ryerson, T. B., Aikin, K. C., de Gouw, J. A., Gilman, J. B., Holloway, J. S., Lerner, B. M., Nadkarni,
510 R., Neuman, J. A., Nowak, J. B., Trainer, M., Warneke, C., and Parrish, D. D.: Quantifying atmospheric
511 methane emissions from the Haynesville, Fayetteville, and northeastern Marcellus shale gas production re-
512 gions, *Journal of Geophysical Research-Atmospheres*, 120, 2119–2139, doi:10.1002/2014JD022697, 2015.

513 Peischl, J., Karion, A., Sweeney, C., Kort, E. A., Smith, M. L., Brandt, A. R., Yeskoo, T., Aikin, K. C., Conley,
514 S. A., Gvakharia, A., Trainer, M., Wolter, S., and Ryerson, T. B.: Quantifying atmospheric methane emis-
515 sions from oil and natural gas production in the Bakken shale region of North Dakota, *Journal of Geophysical*
516 *Research: Atmospheres*, 121, 6101–6111, doi:10.1002/2015jd024631, 2016.

517 Polonsky, I. N., O’Brien, D. M., Kumer, J. B., and O’Dell, C. W.: Performance of a geostationary mission, geo-
518 CARB, to measure CO₂, CH₄ and CO column-averaged concentrations, *Atmospheric Measurement Tech-*
519 *niques*, 7, 959–981, doi:10.5194/amt-7-959-2014, 2014.

520 Rayner, P. J., Utembe, S. R., and Crowell, S.: Constraining regional greenhouse gas emissions using geostation-

521 ary concentration measurements: a theoretical study, *Atmospheric Measurement Techniques*, 7, 3285–3293,
522 doi:10.5194/amt-7-3285-2014, 2014.

523 Rodgers, C. D.: *Inverse Methods for Atmospheric Sounding*, World Scientific, Singapore, 2000.

524 Saunio, M., Bousquet, P., Poulter, B., Peregon, A., Ciais, P., Canadell, J. G., Dlugokencky, E. J., Etiope, G.,
525 Bastviken, D., Houweling, S., Janssens-Maenhout, G., Tubiello, F. N., Castaldi, S., Jackson, R. B., Alexe,
526 M., Arora, V. K., Beerling, D. J., Bergamaschi, P., Blake, D. R., Brailsford, G., Brovkin, V., Bruhwiler, L.,
527 Crevoisier, C., Crill, P., Covey, K., Curry, C., Frankenberg, C., Gedney, N., Hglund-Isaksson, L., Ishizawa,
528 M., Ito, A., Joos, F., Kim, H.-S., Kleinen, T., Krummel, P., Lamarque, J.-F., Langenfelds, R., Locatelli,
529 R., Machida, T., Maksyutov, S., McDonald, K. C., Marshall, J., Melton, J. R., Morino, I., Naik, V., amp,
530 apos, Doherty, S., Parmentier, F.-J. W., Patra, P. K., Peng, C., Peng, S., Peters, G. P., Pison, I., Prigent,
531 C., Prinn, R., Ramonet, M., Riley, W. J., Saito, M., Santini, M., Schroeder, R., Simpson, I. J., Spahni, R.,
532 Steele, P., Takizawa, A., Thornton, B. F., Tian, H., Tohjima, Y., Viovy, N., Voulgarakis, A., van Weele, M.,
533 van der Werf, G. R., Weiss, R., Wiedinmyer, C., Wilton, D. J., Wiltshire, A., Worthy, D., Wunch, D., Xu,
534 X., Yoshida, Y., Zhang, B., Zhang, Z., and Zhu, Q.: The global methane budget 20002012, *Earth System*
535 *Science Data*, 8, 697–751, doi:10.5194/essd-8-697-2016, 2016.

536 Sheng, J.-X., Jacob, D. J., Turner, A. J., Maasackers, J. D., Benmergui, J., Bloom, A. A., Arndt, C., Gautam, R.,
537 Zavala-Araiza, D., Boesch, H., and Parker, R. J.: 2010–2015 methane trends over Canada, the United States,
538 and Mexico observed by the GOSAT satellite: contributions from different source sectors, *Atmospheric*
539 *Chemistry and Physics Discussions*, pp. 1–18, doi:10.5194/acp-2017-1110, 2018a.

540 Sheng, J.-X., Jacob, D. J., Turner, A. J., Maasackers, J. D., Sulprizio, M. P., Bloom, A. A., Andrews, A. E.,
541 and Wunch, D.: High-resolution inversion of methane emissions in the Southeast US using SEAC⁴RS air-
542 craft observations of atmospheric methane: anthropogenic and wetland sources, *Atmospheric Chemistry and*
543 *Physics Discussions*, pp. 1–17, doi:10.5194/acp-2017-1151, 2018b.

544 Skamarock, W. C., Klemp, J. B., Dudhia, J., Gill, D. O., Barker, D. M., Duda, M. G., Huang, X.-Y., Wang, W.,
545 and Powers, J. G.: A Description of the Advanced Research WRF Version 3, Tech. rep., National Center for
546 Atmospheric Research, doi:10.5065/D68S4MVH, 2008.

547 Tan, Z., Zhuang, Q., Henze, D. K., Frankenberg, C., Dlugokencky, E., Sweeney, C., Turner, A. J., Sasakawa, M.,
548 and Machida, T.: Inverse modeling of pan-Arctic methane emissions at high spatial resolution: what can we
549 learn from assimilating satellite retrievals and using different process-based wetland and lake biogeochemical
550 models?, *Atmospheric Chemistry and Physics*, 16, 12 649–12 666, doi:10.5194/acp-16-12649-2016, 2016.

551 Tarantola, A.: *Inverse Problem Theory and Methods for Model Parameter Estimation*, Society for Industrial
552 and Applied Mathematics, Philadelphia, PA, USA, 2004.

553 Turner, A. J. and Jacob, D. J.: Balancing aggregation and smoothing errors in inverse models, *Atmospheric*
554 *Chemistry and Physics*, 15, 7039–7048, doi:10.5194/acp-15-7039-2015, 2015.

555 Turner, A. J., Jacob, D. J., Wecht, K. J., Maasackers, J. D., Lundgren, E., Andrews, A. E., Biraud, S. C.,
556 Boesch, H., Bowman, K. W., Deutscher, N. M., Dubey, M. K., Griffith, D. W. T., Hase, F., Kuze, A.,
557 Notholt, J., Ohyama, H., Parker, R., Payne, V. H., Sussmann, R., Sweeney, C., Velazco, V. A., Warneke,
558 T., Wennberg, P. O., and Wunch, D.: Estimating global and North American methane emissions with high
559 spatial resolution using GOSAT satellite data, *Atmospheric Chemistry and Physics*, 15, 7049–7069, doi:
560 10.5194/acp-15-7049-2015, 2015.

561 Turner, A. J., Jacob, D. J., Benmergui, J., Wofsy, S. C., Maasackers, J. D., Butz, A., Hasekamp, O., and Biraud,
562 S. C.: A large increase in U.S. methane emissions over the past decade inferred from satellite data and surface
563 observations, *Geophysical Research Letters*, pp. 2218–2224, doi:10.1002/2016gl067987, 2016a.

564 Turner, A. J., Shusterman, A. A., McDonald, B. C., Teige, V., Harley, R. A., and Cohen, R. C.: Network
565 design for quantifying urban CO₂ emissions: assessing trade-offs between precision and network density,
566 *Atmospheric Chemistry and Physics*, 16, 13 465–13 475, doi:10.5194/acp-16-13465-2016, 2016b.

567 Turner, A. J., Frankenberg, C., Wennberg, P. O., and Jacob, D. J.: Ambiguity in the causes for decadal trends
568 in atmospheric methane and hydroxyl, *Proc Natl Acad Sci U S A*, 114, 5367–5372, doi:10.1073/pnas.
569 1616020114, 2017.

570 Veefkind, J. P., Aben, I., McMullan, K., Frster, H., de Vries, J., Otter, G., Claas, J., Eskes, H. J., de Haan, J. F.,
571 Kleipool, Q., van Weele, M., Hasekamp, O., Hoogeveen, R., Landgraf, J., Snel, R., Tol, P., Ingmann, P.,
572 Voors, R., Kruizinga, B., Vink, R., Visser, H., and Levelt, P. F.: TROPOMI on the ESA Sentinel-5 Precursor:
573 A GMES mission for global observations of the atmospheric composition for climate, air quality and ozone
574 layer applications, *Remote Sensing of Environment*, 120, 70–83, doi:10.1016/j.rse.2011.09.027, 2012.

575 Wecht, K. J., Jacob, D. J., Frankenberg, C., Jiang, Z., and Blake, D. R.: Mapping of North American methane
576 emissions with high spatial resolution by inversion of SCIAMACHY satellite data, *Journal of Geophysical
577 Research: Atmospheres*, 119, 7741–7756, doi:10.1002/2014jd021551, 2014a.

578 Wecht, K. J., Jacob, D. J., Sulprizio, M. P., Santoni, G. W., Wofsy, S. C., Parker, R., Bsch, H., and Worden, J.:
579 Spatially resolving methane emissions in California: constraints from the CalNex aircraft campaign and from
580 present (GOSAT, TES) and future (TROPOMI, geostationary) satellite observations, *Atmospheric Chemistry
581 and Physics*, 14, 8173–8184, doi:10.5194/acp-14-8173-2014, 2014b.

582 Worden, J. R., Turner, A. J., Bloom, A., Kulawik, S. S., Liu, J., Lee, M., Weidner, R., Bowman, K., Frankenberg,
583 C., Parker, R., and Payne, V. H.: Quantifying lower tropospheric methane concentrations using GOSAT
584 near-IR and TES thermal IR measurements, *Atmospheric Measurement Techniques*, 8, 3433–3445, doi:
585 10.5194/amt-8-3433-2015, 2015.

586 Xi, X., Natraj, V., Shia, R. L., Luo, M., Zhang, Q., Newman, S., Sander, S. P., and Yung, Y. L.: Simulated
587 retrievals for the remote sensing of CO₂, CH₄, CO, and H₂O from geostationary orbit, *Atmospheric Mea-
588 surement Techniques*, 8, 4817–4830, doi:10.5194/amt-8-4817-2015, 2015.

589 Zavala-Araiza, D., Lyon, D. R., Alvarez, R. A., Davis, K. J., Harriss, R., Herndon, S. C., Karion, A., Kort,
590 E. A., Lamb, B. K., Lan, X., Marchese, A. J., Pacala, S. W., Robinson, A. L., Shepson, P. B., Sweeney,
591 C., Talbot, R., Townsend-Small, A., Yacovitch, T. I., Zimmerle, D. J., and Hamburg, S. P.: Reconciling
592 divergent estimates of oil and gas methane emissions, *Proc Natl Acad Sci U S A*, 112, 15 597–602, doi:
593 10.1073/pnas.1522126112, 2015.